Sub Topic: Heterogeneous Combustion

Spring Technical Meeting
Eastern States Section of the Combustion Institute
March 6-9, 2022
Orlando, Florida

Ignition and Combustion of Microcrystalline Cellulose in a Hencken Burner

Parvaneh Motiei[1], Maisha Ahmad[2], Jillian L. Goldfarb[2], Jacqueline O'Connor[1,]*

[1]Mechanical Engineering, Pennsylvania State University, University Park, PA USA
[2] Biological and Environmental Engineering, Cornell University, Ithaca, NY USA
[*]Corresponding Author Email: jxo22@psu.edu

The present study explores the combustion of microcrystalline cellulose as a model solid biofuel. Particles with a nominal diameter of 75 μm were burned in a Hencken burner in an H_2/air atmosphere. CH* chemiluminescence imaging and particle image velocimetry were conducted to measure ignition delay time and volatile burning time. A series of repeatability tests were carried out to demonstrate a rigorous uncertainty analysis for both ignition delay time and volatile burning time. An equivalence ratio of 0.3 was the lowest ignition limit, where ignition and volatile burning times varied greatly because of low co-flow temperature. Ignition delay time decreases as the equivalence ratio increases, suggesting that ignition delay time is more strongly influenced by the co-flow temperature than by O_2 concentration in the surrounding gas. Volatile burning time was not a strong function of equivalence ratio. These combustion studies were paired with thermogravimetric analysis (TGA) to assess the composition of microcrystalline cellulose (MCC) and the rate of mass loss as functions of time and temperature. Unlike many solid fuels, cellulose leaves no char after burnout; this result was expected as the proximate analysis of pure cellulose shows the composition to be ~98% volatile matter, ~1.7% fixed carbon, and ~ 0.3 % ash. TGA aligns with the observation that the volatile burning time is not significantly influenced by equivalence ratio, in that the cellulose has a high peak reactivity and is oxidized completely at relatively low temperatures.

Keywords: Microcrystalline cellulose, Ignition, Devolatilization, Biofuel combustion

1. Introduction

Achieving deep decarbonization goals will likely require the integration of biomass-based fuels into conventional power- and heat-generation systems. While biomass combustion emits fewer hazardous air pollutants than its fossil fuel counterparts and could approach a net-zero CO_2 impact [1], direct combustion of solid biomass faces several challenges related to combustion efficiency and flame stabilization. Overcoming these challenges requires a comprehensive understanding of biomass combustion behavior from devolatilization to ignition through burn-out [2,3]. Prior research investigates the ignition delay time and volatile burning time scales for raw biomass and coal with the goal to make biomass combustion comparable with coals, as biomass is often considered to be a drop-in replacement for coal [2,4–12].

While both coal and biomass are carbonaceous solids, there are two primary differences between these fuels: their composition and their physical structure across scales. Lignocellulosic biomasses tend to have higher elemental oxygen and hydrogen content, fewer aromatics, lower

porosity, higher moisture content, higher oxidative reactivities and lower heating values than coals, especially bituminous and higher ranked coals [13]. Five processes govern combustion of solid carbon-based particles [3]: particle heating, devolatilization, combustion of volatile gases, char formation, and char burnout. The details of each of these processes, including their rates and efficiencies, is highly dependent on the elemental content and physical structure of the particles, as well as the heating rate of the particle [14]. In general, biomass exihibts shorter devolatilization times as compared to coal [15]. Despite coal having a higher thermal conductivity [16,17], biomass has a considerably higher volatile matter content comprised of fewer aromatics and other carbon-condensed organics, leading to a more rapid pyrolysis that begins at lower temperatures [18]. Such observations continue for ignition delay time; single-particle combustion experiments of pulverized sugarcane bagasse and three different rank coal show shorter ignition delay times for the biomass particles [6].

Fuel science routinely uses thermogravimetric analysis (TGA) to describe thermal decomposition (both pyrolysis and oxidation) behavior in terms of relative reactivity and "combustibility" of solid fuels [15,19–26]. While TGA heating conditions are considerably slower (heating rates less than 100 K/min) than an industrial combustor, or even the Hencken burner used here, it is widely argued that such studies provide a reliable quantitation of thermochemical processes, as the sample mass heating rate to particle ratios are reasonably scalable [27]. Given the drastic impacts of heating rate on the combustion process [28,29], it is critical to simultaneously investigate the oxidation of biomass using TGA *and* combustion experiments, as the particle heating rates in flames are orders of magnitude higher than those in TGA.

Combining combustion studies with TGA provides insight into the oxidation of biomasses critical to their application as green energy feedstocks [30–32]. Single-particle biomass combustion experiments, conducted in parallel with TGA, were used to assess the self-ignition risk of biomass during storage and transportation [30]. Volatile ignition temperature and particle ignition temperature were obtainted using a heating rate of 20 K/min using TGA, while ignition delay time and ignition mode data were obtained by burning the particles in an entrained flow reactor (EFR) under higher heating rates (~10^5 K/s) to resemble ignition under realistic heating conditions. The ignition temperatures obtained from TGA were 200-300 K lower than those measured from EFR, as the ignition criterion are different in these two types of experiments. The authors of this study attribute the difference in ignition temperatures to the TGA study being kinetically controlled, while in combustion the reaction is O_2-diffusion controlled. Li et al. [32] studied the ignition behavior of woody biomasses in a down-fire furnace accompanied by TGA data. They suggested that although TGA showed that the presence of O_2 hastens the devolatilization process, it failed to reveal the impact of particle size on biomass ignition behavior as a result of the low heating rate and lack of motion of particles in the TGA. However, it is difficult to determine whether this behavior was due to enhanced devolatilization or if the volatiles and char surface underwent (at least partial) oxidation in the presence of air versus N_2.

The present work provides a proof-of-concept of several key experiments and analysis techniques required to couple combustion and TGA experiments for longer-term biomass studies. Pure cellulose ignites at lower temperatures compared to lignocellulosic biomasses; the interplay between the presence of lignin and hemicellulose and their structural linkages with cellulose delay the ignition process [33]. However, Wang et al. [34] studied the ignition behavior of the three major model components and five representative biomasses in a drop tube furnace, concluding that although the ignition mechanism of biomass highly depends on the lignin content, the ignition temperature is mainly influenced by cellulose fraction. As such, cellulose is used in this work as a

model biomass compound to validate and quantify the uncertainty of combustion studies and provide a basis for aligning data from the combustion and fuel science communities. We find that TGA results can provide useful insight into the role of rate-limiting processes as well as information about the mass loss rate of solid biofuels in controlled environments.

2. Methods / Experimental Setup

2.1. Burner setup

The combustion experiment is performed using a Hencken burner with a central tube for particle injection to characterize the combustion of microcrystalline cellulose. The schematic shown in Figure 1 illustrates the front view of the burner, including the fuel (H_2), oxidizer (air), and particle inlet ports. All gases, including air, H_2, and N_2, are metered using rotameters. Fuel and oxidizer are injected through two ports to the lower and upper rings, respectively. Air flows to the surface of the burner through a steel honeycomb structure and H_2 reaches the burner surface through 84 stainless steel tubes of 1 mm diameter each. The small laminar diffusion flamelets merge to create a flat flame. Using a fluidized bed seeder, the solid fuel particles, nominally 75 µm in diameter, are entrained by a carrier gas (N_2) flowing through the central port in the bottom of the burner. The burner is enclosed by a 35.56 mm diameter quartz tube with optical access to prevent entrainment of outside air and disturbances to the flame and particle stream.

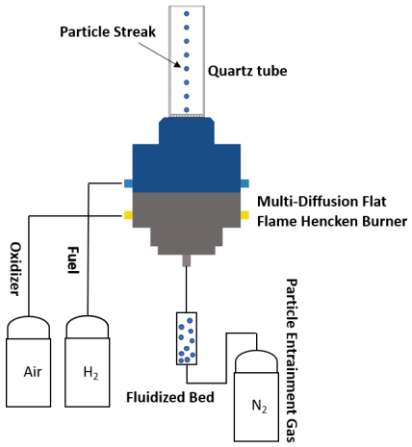

Figure 1: Schematic of the experimental rig and flow diagram

2.2. Cellulose Feedstock

Cellulose is often used as a model biomass compound given its homogeneity and prevalence in biomass [35]. The proximate analysis of the microcrystalline cellulose ($C_{12}H_{22}O_{11}$, Alfa Aesar) investigated in this study is given in

Table *1* determined by TGA [36].

Table 1: Proximate analysis of cellulose (± standard deviation)

Component	Weight Percent – Dry Basis
Ash-Dry Basis (wt %)	0.34 ± 0.48
Fixed Carbon-Dry Basis (wt %)	1.7 ± 0.25
Volatile Matter-Dry Basis (wt %)	97.95± 0.73

2.3. Combustion Diagnostics

Two combustion diagnostics were used to quantify the ignition delay time and burnout time of the cellulose particles: chemiluminescence imaging and particle image velocimetry.

2.3.1. Chemiluminescence imaging

CH* chemiluminescence imaging was performed to identify the different stages of particle combustion, from ignition to burnout. CH* chemiluminescence was imaged using a PI-MAX (Gen II) intensified camera with a Nikon 50 mm f /1.4, filtered using a 430 nm +/- 10 nm filter (Andover Corporation) The gain and exposure time were 75 and 1.3 seconds per image, respectively. In order to statistically analyze the data, 100 images were obtained for each condition and each test was repeated six times to gauge repeatability. Figure 2 shows an example of a time-averaged CH* chemiluminescence image of cellulose particle combustion and the corresponding centerline signal intensity profile versus the height above the burner surface for 100 images.

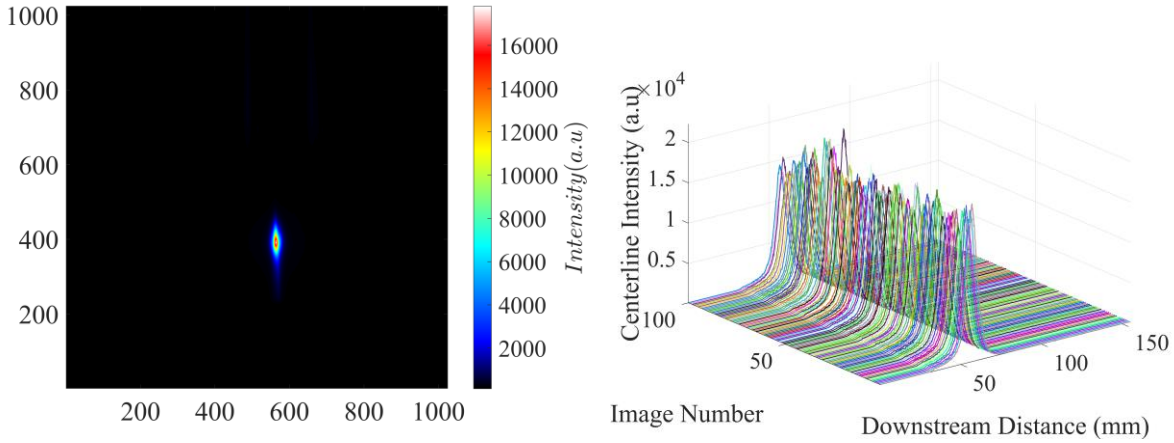

(a) (b)

Figure 2: Example of a) time-averaged CH* chemiluminescence image of microcrystalline cellulose particles and b) intensity signal of the centerline for microcrystalline cellulose particles from CH* chemiluminescence for 100 separate images at $\phi = 0.4$

The centerline intensity signal profile provides information about the sequence of the particle combustion steps. After the particle is injected into the burner, it is heated by the surrounding gases from the hydrogen-air flat flame. During this heating process, devolatilization commences and volatile gases leave the particle and mix with the oxygen-containing surrounding gases. After sufficient devolatilization and the ignition delay time of the gaseous mixture lapses, the gaseous mixture ignites. Upon ignition, volatile gases burn in the surrounding oxidative environment. Devolatilization and combustion of volatile gases continues until the particles are completely devolatilized and the diffusion flame is extinguished. Upon flame extinction, depending on whether there is char residue left or not, heterogenous combustion of char particles begins at this stage. *Figure 3* shows an example of the centerline intensity profile analysis that is used to determine the ignition delay time and burnout time. The combustion zone is bounded by the ignition location, x_1, and volatile burning end location, x_2. The ignition location, x_1, is defined as the location where the centerline intensity profile reaches the 50% of its maximum value. The volatile burning distance ($x_2 - x_1$) is defined by the full-width half-max (FWHM) of the centerline

intensity curve. These length scales can be converted into the corresponding time scales – the ignition delay time, τ_{ig}, and volatile burning time, τ_b - using the jet particle velocity, as described below. Repeatability studies were conducted as described in Section 3.2.

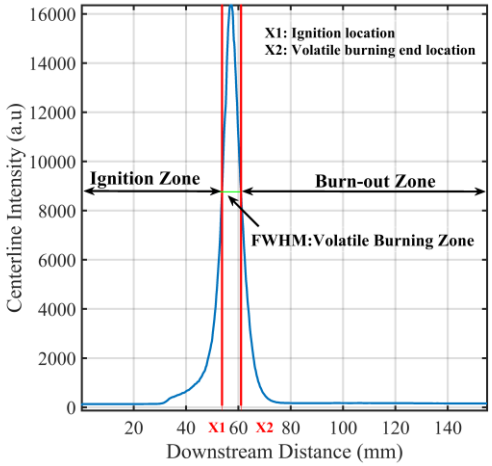

Figure 3: Example of intensity analysis of a time-averaged CH* chemiluminescence image

2.3.2. Particle image velocimetry

Particle velocity is measured using particle image velocimetry (PIV), where this velocity is used in combination with the CH* chemiluminescence images to calculate key combustion timescales. The PIV setup contains a dual-cavity, diode-pumped, solid-state laser (Hawk-Duo-532-60-M/Rev.A at 532 nm) and a high-speed CMOS camera (FASTCAM SA1.1). The laser beam passes through a LaVision sheet-forming optic with a focal length of f=-10 mm, forming a laser sheet that is aligned with the central tube of the burner. The camera is positioned perpendicular to the laser sheet and a 60 mm macro lens is used to provide a narrow field of view and a higher magnification of the jet of particles. The PIV domain size is 120 mm in the streamwise direction and 36 mm in the cross-stream direction. PIV images are taken at 5 kHz and 768×768 pixel resolution. Laser pulse time separation is $dt = 35\,\mu s$. LaVision DaVis 8.4 cross-correlation algorithm is used for the velocity calculation. Velocity vectors are computed in a 16x16 pixels interrogation window with 50% overlap, resulting in a vector spacing of 1.17 mm. The uncertainty of the mean velocity is 0.005-0.11 m/s in the jet core, using the DaVis uncertainty calculation algorithm.

τ_{ig} and τ_b are calculated using the centerline intensity profile from the CH* chemiluminescence images and the centerline velocity data from PIV as defined in Eqs (1-2):

$$\tau_{ig} = \sum_{i=1}^{i=x_1} \frac{x_{i+1} - x_i}{u_i} \qquad (1)$$

$$\tau_b = \sum_{i=x_1}^{i=x_2} \frac{x_{i+1} - x_i}{u_i} \qquad (2)$$

In Equations 1 and 2, x_i and u_i are the location and particle velocity in the discretized region along the streamwise direction, respectively. Figure 5 shows an example centerline velocity calculation with the ignition location and burn-out zone indicated in vertical red lines.

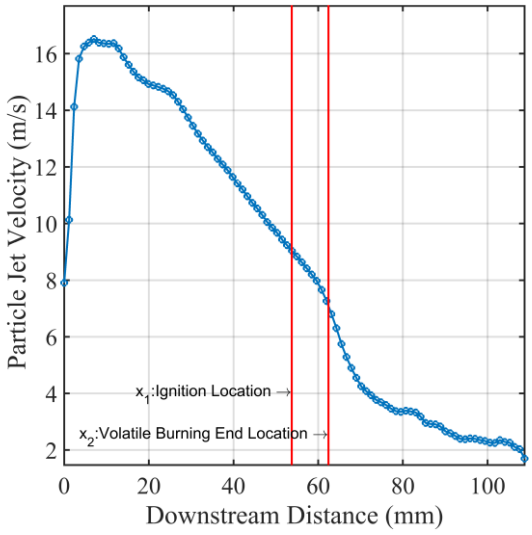

Figure 4: Example of superimposition of length scales obtained from CH* chemiluminescence imaging on particle jet velocity profile

2.3.3. Thermal Analysis of Microcrystalline Cellulose

In addition to the combustion experiments, samples were analyzed on a TA Instruments Discovery series 650 thermogravimetric analyzer (TGA) under different heating profiles and atmospheres to obtain the composition and mass loss dependence on temperature. Between 10-15 mg of sample is loaded into a 70 μL alumina crucible. The TGA is run in two modes: pyrolysis (used to determine proximate analysis in Table 1) and oxidation. For the pyrolysis runs, the sample is heated from room temperature to 110℃ at a rate of 10℃ per minute under a high-purity nitrogen atmosphere and held for 30 minutes to drive off moisture. Next, the sample is heated to 900℃, again at a rate of 10℃ per minute under N_2, and held at 900°C for 30 minutes. This mass loss during this process is attributed to devolitalization. To complete the proximate analysis, the sample is exposed to dry air and heated to 950℃ at a rate of 10℃ per minute and held for an additional 30 minutes; the mass lost in this final step is fixed carbon and non-organic residual matter termed "ash."

To explore the oxidative behavior as a function of heating rate – what the fuel science literature often refers to as "combustion" in TGA – the samples are run in a dry air atmosphere. The sample is heated to 110°C at 10°C/min and held for 30 minutes to establish a dry baseline starting mass, and and then the sample then heated to 950°C at five different heating rates and then held for 30 minutes. Eleven TGA runs in air were performed for five different heating rates (at 5, 10, 25, 50 and 100℃/min), with triplicates performed for 5℃/min, 50℃/min, and 100℃/min runs. During the TGA runs, the mass of the sample and temperature are recorded every 0.5 s, which allows for the construction of a derivative thermogravimetric (DTG) curve illustrating the mass loss rate as a function of time. The percent mass at any time t, $X(t)$, during this process was determined using the following equation:

$$X(t) = \left(\frac{m_{initial} - m_t}{m_{initial} - m_{final}}\right) \qquad (3)$$

In Equation 3, $m_{initial}$ is the initial dry sample mass after the hold at 110°C, m_t is the mass at each time, t, and m_{final} is the mass of the exhausted sample after the temperature ramp. For pyrolysis DTG curves, this represents the mass after the hold at 900°C in N_2 and for oxidation curves after the hold in air at 950°C. The DTG curve is constructed by plotting dX/dt versus temperature.

3. Results and Discussion

3.1.Test matrix

The text matrix includes five equivalence ratios for the H_2/air flames and one particle flow rate. The entrainment gas flow rate was kept to 0.38 slpm, which was the minimum flow rate to provide continuous particle fluidization. The adiabatic flame temperature, T_{ad}, and product oxygen concentration for the co-flow flames in the Hencken burner were calculated using GRIMech 3.0 and the equilibrium solver in Chemkin; results are shown in Table 2. As the equivalence ratio increases, the surrounding gas temperature increases, which would tend to reduce ignition delay and burnout times. However, as equivalence increases, the oxygen concentration decreases, which should have the opposite effect. In future studies, the temperature and oxygen concentration effects will be controlled separately by blending oxygen with different diluents, but the results in this initial study show the compounding effects of varying temperature and oxygen concentration.

Table 2: Calculated T_{ad} and product O_2 concentration

φ	Air (slpm)	H_2 (slpm)	T_{ad} (K)	O_2 mole fraction
0.3	18.16	2.32	1186	0.13
0.35	18.16	2.71	1308	0.12
0.4	18.16	3.10	1424	0.11
0.45	18.16	3.48	1535	0.10
0.5	18.16	3.87	1640	0.09

3.2. Repeatability in CH chemiluminescence and velocity diagnostics*

Statistical repeatability tests were carried out on both CH* chemiluminescence imaging and velocity measurements from PIV. Six different CH* image datasets taken over multiple days for each condition and were processed to determine two quantities used in the calculation of the ignition delay time and volatile burning time: the ignition location, which is where the centerline intensity equals 50% of the peak signal intensity, and the volatile burnout distance, which is the FWHM of the centerline signal. In the present study, we use the median as the measure of central tendency and the inner-quartile range (IQR) as a measure of statistical dispersion [37]. Boxplots of an example condition, $\phi = 0.4$, are shown in Figure 5. The median is indicated by the red horizontal line and the inner-quartile range is indicated by the extent of the blue boxes. The black horizontal lines above and below the blue boxes indicate the maximum and minimum values of each data set, and the red crosses are outliers, which are defined as points greater than 1.5IQR from the median. The overlapping IQR indicates that the difference among datasets is not statistically significant.

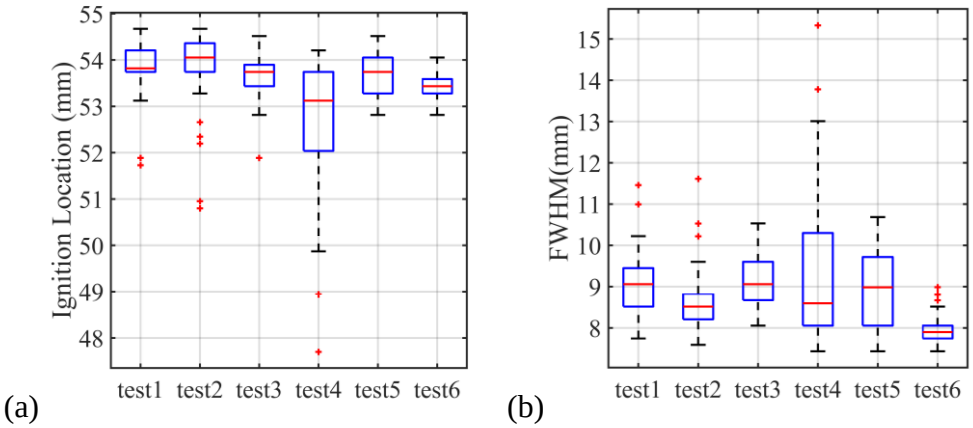

(a) (b)

Figure 5: Boxplots for (a) ignition location and (b) FWHM at $\phi = 0.4$

Out of all the operating conditions shown in Table 2, only the $\phi = 0.3$ condition was not repeatable. Figure 6 shows the repeatability results for the ignition location and FWHM at this equivalence ratio, which indicates the significant variation in ignition delay location for this condition and the large number of outliers. This result indicates the lower bound for ignition of these particles, where the surrounding temperature of T_{ad}=1186 K is not high enough to reliably ignite the particles. Further, there is a significantly larger FWHM IQR at $\phi = 0.3$ in Figure 6 as compared to that for $\phi = 0.4$ in Figure 5 (note the difference in y-axis labels), which indicates much longer and more variable volatile burning times. Visual observation of this condition showed that some particles are not burned. As such, the remainder of the analysis considers equivalence ratios of $\phi = 0.35$ and above, where reliable and repeatable ignition occurs.

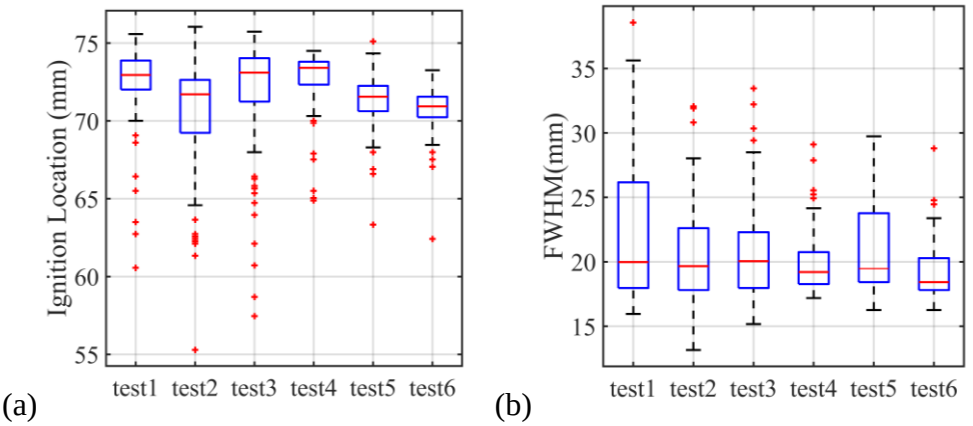

(a) (b)

Figure 6: Boxplots for (a) ignition location and (b) FWHM at $\phi = 0.3$

The repeatability of the velocity measurements was also tested across multiple days; Figure 7 shows the results of five repeated tests for an example condition, $\phi = 0.4$, all of which are quantitatively similar. Similar repeatability was ensured in all cases. The ignition and the end of volatile burning locations obtained from CH* chemiluminescence imaging are shown by red vertical lines in the figure. Once the particles are injected into the burner, the particle jet velocity increases because of the momentum of the hot environment around it. After the particles reach their maximum value, they decelerate until the particles burn out and can no longer be tracked. In

the calculation of τ_{ig} and τ_b , the velocity profiles used in Eqs (1-2) are obtained by taking the median value of the five repeated velocity profiles at each downstream distance.

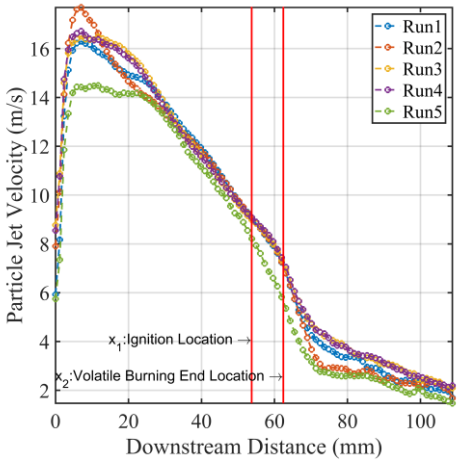

Figure 7: Microcrystalline cellulose particle velocity profile along the downstream distance for five different repeats at $\phi = 0.4$

3.3. Ignition delay time and volatile burning time

The ignition delay times and volatile burning times are shown in Figure 8 (a) and (b), respectively. Results show that increasing the equivalence ratio, accompanied by increasing T_{ad}, results in a shorter ignition delay time, from 5.2 $msec$ at $\phi = 0.35$ to 2.7 $msec$ at $\phi = 0.5$. The uncertainty in the ignition delay time is relatively constant across all operating conditions. These results show that ignition delay time is largely a function of temperature, not O_2 concentration, as the ignition timescales decrease with increasing temperature but decreasing oxygen concentration. The volatile burning time is largely independent of the equivalence ratio of the flat flame, and the uncertainty of the volatile burning time is slightly higher for $\phi = 0.35$ as compared to the other conditions.

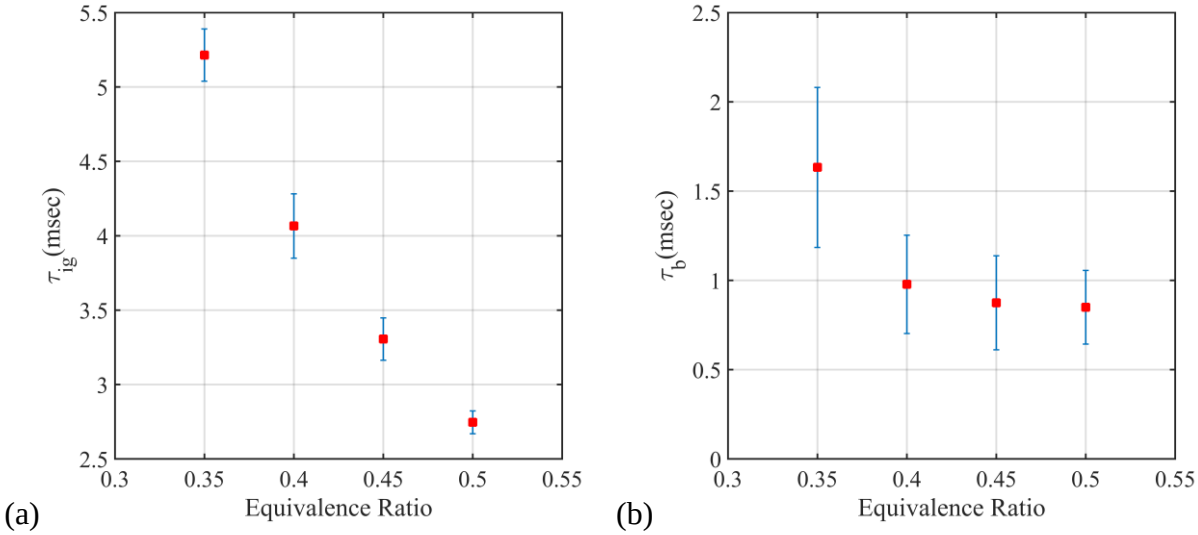

Figure 8: (a) Ignition delay time (b) volatile burning time of microcrystalline cellulose particles vs. equivalence ratio

The measurement uncertainty was evaluated using multivariable uncertainty analysis. The uncertainty in τ_{ig} is driven by the variability in x_1 and the velocity profile, u. The uncertainty in τ_b is driven by the uncertainties in measurements of x_1, x_2, and u. The uncertainties are presented in Table 3. The uncertainties in the burnout time are large relative to the burnout time itself. The uncertainty arises from variations in the FWHM of the chemiluminescence signal rather than variations in the velocity measurements in this region, as can be seen by inspecting the variability in these quantities Figure 5 and Figure 7.

Table 3: Meaurment unceraintity for ignition delay time τ_{ig} , and volatile burning time τ_b

	φ =0.35	φ =0.4	φ =0.45	φ =0.5
Uncertainty in τ_{ig}(%)	3.37	5.31	4.28	2.79
Uncertainty in τ_b(%)	27.43	28.18	30.12	24.35

3.4. TGA results

One of the primary criticisms of using TGA oxidation data to represent combustion behavior is the slow heating rates experienced by samples, upon which reaction rates depend [38]. This limitation is shown in Figure 9, where on the left we plot the fraction of cellulose remaining in the cruicible as a function of reaction time and on the right as a function of TGA furnace temperature in an air environment.

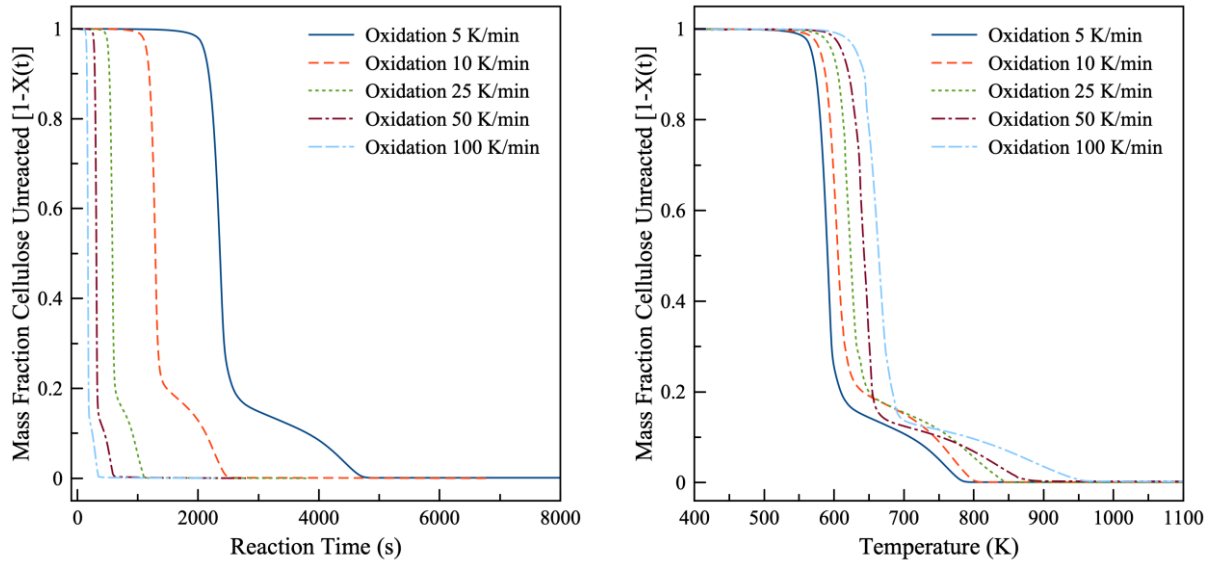

(a) (b)

Figure 9 : (a) Normalized mass loss as a function of time and (b) furnace temperature for oxidation of microcrystalline cellulose at five heating rates in an air environment.

The time required for complete oxidation is inversely proportional to reaction rate; while complete oxidation occurs at higher temperatures for higher heating rates, the rate of decomposition is faster at higher heating rates. This is due to the residence time of the cellulose particles; at 5 K/min the particles decompose (devolatilize/oxidize) at lower temperatures than at

the 100 K/min ramp rate because they remain at each temperature longer. In both the time-based and temperature-based curves, the decomposition occurs in two stages: a stage of very rapid mass loss where approximately 80% of the mass is lost for all cases, and then a slower mass loss regime where the remaining 20% of the mass decomposes.

The mass loss dependence on heating rate is further highlighted in the DTG curves of Figure 10. The DTG curves show that maximum mass loss rate increases as the heating rate increases; the sample is more reactive at higher temperatures. The same onset of mass loss lag noted in Figure 9a is mirrored in the DTG curves of Figure 10; the particles take longer at slower heating rates to reach a temperature at which they begin to devolatilize/oxidize.

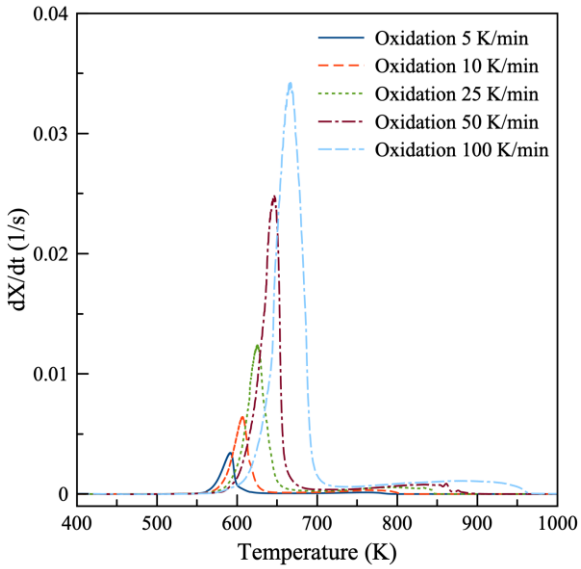

Figure 10 : DTG curves for (a) oxidation of microcrystalline cellulose at five heating rates in an air environment.

Pyrolysis TGA runs with a nitrogen environment were used to probe the two-stage or two-regime behavior noted as shoulder peaks in Figure 9 (between 600 and 900 K). Figure 11 compares the mass loss curves for the air (labeled oxidation) and nitrogen (labeled pyrolysis) environments for three heating rates. As shown in Figure 11a, the onset and mass loss (and corresponding temperature) for pyrolysis and oxidation are roughly equal at 5 and 10 K/min. There is some slight separation beginning to occur at 50 K/min (future work will examine 100 K/min data) where the cellulose reacts sooner (at lower temperature) under an air atmosphere than nitrogen.

In the DTG curves of Figure 11b, we can clearly see that for each temperature ramp rate, the mass loss begins at slightly lower temperatures for oxidation than pyrolysis. The maximum mass loss rate, found at the peak of the DTG curves (often used in fuel science as a guage of reactivity) is slightly higher for oxidation than pyrolysis, and the peak temperature slightly lower for oxidation than pyrolysis. Despite these differences, the initial decomposition of the samples in both air and nitrogen atmospheres are relatively similar. They are both very rapid and, according to the DGT, have similar initial slopes.

This combination of results suggests that devolatilization requires more energy (heat input) than oxidation; oxidation is an exothermic process (at least under these conditions) so it is likely that the volatiles released from the cellulose are oxidizing in the air atmosphere, supplying additional energy to sustain the pyrolysis/oxidation process. This interplay between temperature

and heating rate noted in the DTG curves provides insight into the data found in Figure 8, namely that the ignition delay time decreases as adiabatic flame temperature increases. The heating rate and flame temperatures are considerably higher than those used in the TGA, and the trends in TGA data suggest that at such high temperatures the mass conversion rate (due to both pyrolysis and oxidation) are orders of magnitude higher than that observed here. However, these results tell us that even at low temperatures, the pyrolysis process is somewhat comparable to the oxidation process, meaning that microcrystalline cellulose likely decomposes very quickly at combustion-relevant temperatures. We hypothesize, therefore, that the differences in ignition delay time seen in Figure 8 may be a gas kinetic effect, not a decomposition effect.

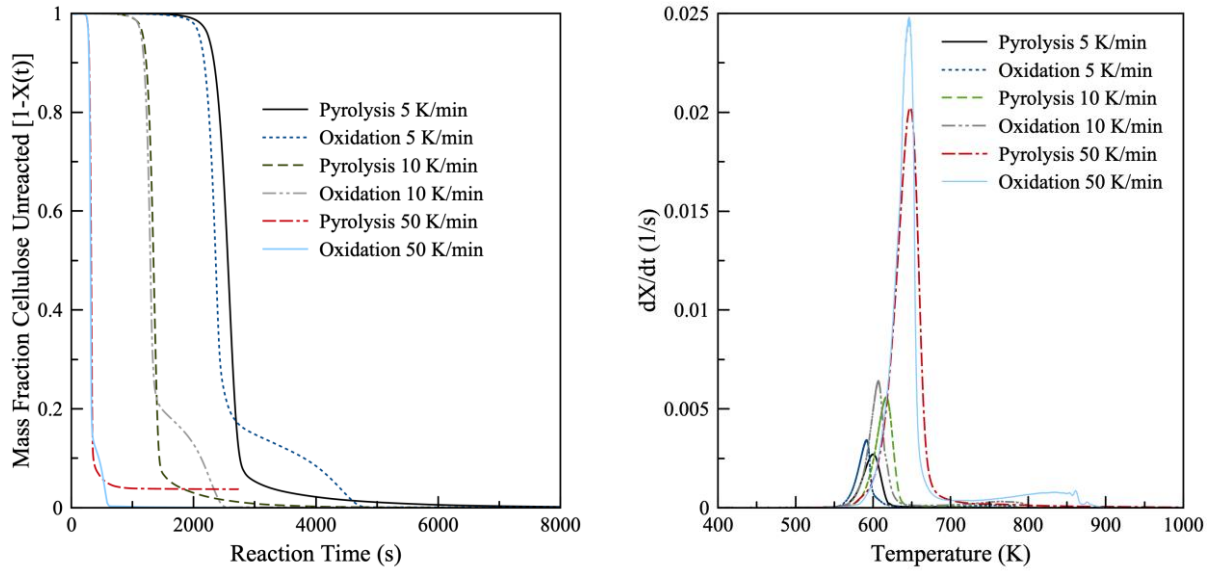

(a) (b)

Figure 11 : Pyrolysis and oxidation of cellulose at 5, 10 and 50 K/min observed through (a) fractional conversion and (b) DTG curves

On-going work includes particle ignition temperature measurements using two-color pyrometery to use as a comparative metric against TGA ignition and burn-out temperatures, as well as differential scanning calorimetry studies to understand the impact of heat transfer on the pyrolysis and oxidation steps.

4. Conclusions

In this experimental study, microcrystalline cellulose particles were burned in a Hencken burner under H_2/air atmosphere to characterize the ignition and burnout of this material. CH* chemiluminescence imaging and particle image velocimetry were used to observe and quantify the combustion behavior of particles. The ignition delay time decreased with increasing equivalence ratio, showing that in this experiment, ignition delay time is a stronger function of temperature than O_2. Burnout time is not considerably influenced by equivalence ratio. No char was observed after the burnout stage, which was expected based on the proximate analysis resulted in about 98% volatile matter content, 1.71% fixed carbon, and 0.3 % ash. The TGA results showed that cellulose decomposition in both air and nitrogen environments is more rapid at higher heating rates. Decomposition happens slightly earlier and faster in oxidation environments, but the pyrolysis

process is also quite rapid at the heating rates considered. Future work will compare the decomposition temperatures in the TGA and temperatures measured in the combustion experiment using two-color pyrometry.

5. Acknowledgments

This work was supported by the National Science Foundation grant CBET-2031710. Any opinions, findings, conclusions, or recommendations expressed in this material are those of the authors and do not necessarily reflect the views of the National Science Foundation.

6. References

[1] Emenike O, Michailos S, Finney KN, Hughes KJ, Ingham D, Pourkashanian M. Initial techno-economic screening of BECCS technologies in power generation for a range of biomass feedstock. Sustain Energy Technol Assessments 2020;40:100743. https://doi.org/10.1016/j.seta.2020.100743.

[2] Fatehi H, Schmidt FM, Bai XS. Gas phase combustion in the vicinity of a biomass particle during devolatilization – Model development and experimental verification. Combust Flame 2018;196:351–63. https://doi.org/10.1016/j.combustflame.2018.06.025.

[3] Nussbaumer T. Combustion and Co-combustion of Biomass: Fundamentals, Technologies, and Primary Measures for Emission Reduction. Energy and Fuels 2003;17:1510–21. https://doi.org/10.1021/ef030031q.

[4] Yang YB, Yamauchi H, Nasserzadeh V, Swithenbank J. Effects of fuel devolatilisation on the combustion of wood chips and incineration of simulated municipal solid wastes in a packed bed☆. Fuel 2003;82:2205–21.

[5] Ryu C, Yang Y Bin, Khor A, Yates NE, Sharifi VN, Swithenbank J. Effect of fuel properties on biomass combustion: Part I. Experiments—fuel type, equivalence ratio and particle size. Fuel 2006;85:1039–46.

[6] Levendis YA, Joshi K, Khatami R, Sarofim AF. Combustion behavior in air of single particles from three different coal ranks and from sugarcane bagasse. Combust Flame 2011;158:452–65.

[7] Khatami R, Stivers C, Joshi K, Levendis YA, Sarofim AF. Combustion behavior of single particles from three different coal ranks and from sugar cane bagasse in O2/N2 and O2/CO2 atmospheres. Combust Flame 2012;159:1253–71.

[8] Bu C, Leckner B, Chen X, Pallarès D, Liu D, Gómez-Barea A. Devolatilization of a single fuel particle in a fluidized bed under oxy-combustion conditions. Part A: Experimental results. Combust Flame 2015;162:797–808. https://doi.org/10.1016/j.combustflame.2014.08.015.

[9] Shan F, Lin Q, Zhou K, Wu Y, Fu W, Zhang P, et al. An experimental study of ignition and combustion of single biomass pellets in air and oxy-fuel. Fuel 2017;188:277–84. https://doi.org/10.1016/j.fuel.2016.09.069.

[10] Yan H, Fujita O. Study of the transient combustion of highly densified biomass briquette (Bio-coke) in an air flow. Fuel 2017;188:595–602. https://doi.org/10.1016/j.fuel.2016.10.079.

[11] Simões G, Magalhães D, Rabaçal M, Costa M. Effect of gas temperature and oxygen concentration on single particle ignition behavior of biomass fuels. Proc Combust Inst 2017;36:2235–42. https://doi.org/10.1016/j.proci.2016.06.102.

[12] Fatehi H, Weng W, Costa M, Li Z, Rabaçal M, Aldén M, et al. Numerical simulation of ignition mode and ignition delay time of pulverized biomass particles. Combust Flame 2019;206:400–10. https://doi.org/10.1016/j.combustflame.2019.05.020.

[13] Demirbas A. Combustion characteristics of different biomass fuels. Prog Energy Combust Sci 2004;30:219–30. https://doi.org/10.1016/j.pecs.2003.10.004.

[14] Jenkins BM, Baxter LL, Miles TR, Miles TR. Combustion properties of biomass. Fuel Process Technol 1998;54:17–46. https://doi.org/10.1016/S0378-3820(97)00059-3.

[15] Celaya AAM, Lade ATA, Goldfarb JJL. Co-combustion of brewer's spent grains and Illinois No. 6 coal: Impact of blend ratio on pyrolysis and oxidation behavior. Fuel Process Technol 2015;129:39–

51. https://doi.org/10.1016/j.fuproc.2014.08.004.
[16] Herrin JM, Deming D. Thermal conductivity of US coals. J Geophys Res Solid Earth 1996;101:25381–6.
[17] Mason PE, Darvell LI, Jones JM, Williams A. Comparative Study of the Thermal Conductivity of Solid Biomass Fuels. Energy and Fuels 2016;30:2158–63. https://doi.org/10.1021/acs.energyfuels.5b02261.
[18] Wan K, Wang Z, He Y, Xia J, Zhou Z, Zhou J, et al. Experimental and modeling study of pyrolysis of coal, biomass and blended coal-biomass particles. Fuel 2015;139:356–64. https://doi.org/10.1016/j.fuel.2014.08.069.
[19] Goldfarb JL, Liu C. Impact of blend ratio on the co-firing of a commercial torrefied biomass and coal via analysis of oxidation kinetics. Bioresour Technol 2013;149:208–15. https://doi.org/10.1016/j.biortech.2013.09.053.
[20] Dou G, Goldfarb JL. In situ upgrading of pyrolysis biofuels by bentonite clay with simultaneous production of heterogeneous adsorbents for water treatment. Fuel 2017;195:273–83. https://doi.org/10.1016/j.fuel.2017.01.052.
[21] Işıtan S, Ceylan S, Topcu Y, Hintz C, Tefft J, Chellappa T, et al. Product quality optimization in an integrated biorefinery: Conversion of pistachio nutshell biomass to biofuels and activated biochars via pyrolysis. Energy Convers Manag 2016;127:576–88. https://doi.org/10.1016/j.enconman.2016.09.031.
[22] Patnaik AS, Goldfarb JL. Continuous activation energy representation of the Arrhenius equation for the pyrolysis of cellulosic materials: Feed corn stover and cocoa shell biomass. Cellul Chem Technol 2016;50.
[23] Aboulkas A, El harfi K, El Bouadili A. Thermal degradation behaviors of polyethylene and polypropylene. Part I: Pyrolysis kinetics and mechanisms. Energy Convers Manag 2010;51:1363–9. https://doi.org/10.1016/j.enconman.2009.12.017.
[24] Melendi-Espina S, Alvarez R, Diez MA, Casal MD. Coal and plastic waste co-pyrolysis by thermal analysis-mass spectrometry. Fuel Process Technol 2015;137:351–8. https://doi.org/10.1016/j.fuproc.2015.03.024.
[25] Huang YF, Kuan WH, Chiueh PT, Lo SL. Pyrolysis of biomass by thermal analysis – mass spectrometry (TA – MS). Bioresour Technol 2011;102:3527–34. https://doi.org/10.1016/j.biortech.2010.11.049.
[26] López F, Hadad A El, Alguacil F, Centeno T. Kinetics of the Thermal Degradation of Granulated Scrap Tyres: a Model-free Analysis. Mater Sci 2013.
[27] Vamvuka D, Sfakiotakis S. Combustion behaviour of biomass fuels and their blends with lignite. Thermochim Acta 2011;526:192–9. https://doi.org/10.1016/j.tca.2011.09.021.
[28] Yu J, Lucas JA, Wall TF. Formation of the structure of chars during devolatilization of pulverized coal and its thermoproperties: A review. Prog Energy Combust Sci 2007;33:135–70. https://doi.org/10.1016/j.pecs.2006.07.003.
[29] Anthony DB, Howard JB. Coal devolatilization and hydrogastification. AIChE J 1976;22:625–56. https://doi.org/10.1002/aic.690220403.
[30] Magalhães D, Kazanç F, Ferreira A, Rabaçal M, Costa M. Ignition behavior of Turkish biomass and lignite fuels at low and high heating rates. Fuel 2017;207:154–64. https://doi.org/10.1016/j.fuel.2017.06.069.
[31] Mason PE, Darvell LI, Jones JM, Pourkashanian M, Williams A. Single particle flame-combustion studies on solid biomass fuels. Fuel 2020;151:21–30. https://doi.org/10.1016/j.fuel.2014.11.088.
[32] Li J, Paul MC, Czajka KM. Studies of Ignition Behavior of Biomass Particles in a Down-Fire Reactor for Improving Co-firing Performance. Energy and Fuels 2016;30:5870–7. https://doi.org/10.1021/acs.energyfuels.6b01065.
[33] Particles A, Urban JL, Engineering M. Spot Fire Ignition of Natural Fuels by Hot. Fire Technol 2018;54:797–808. https://doi.org/10.1007/s10694-018-0712-4.
[34] Wang S, Zou C, Lou C, Yang H, Mei M, Jing H, et al. Bioresource Technology Effects of

hemicellulose , cellulose and lignin on the ignition behaviors of biomass in a drop tube furnace. Bioresour Technol 2020;310:123456. https://doi.org/10.1016/j.biortech.2020.123456.

[35] Zong P, Jiang Y, Tian Y, Li J, Yuan M, Ji Y, et al. Pyrolysis behavior and product distributions of biomass six group components: Starch, cellulose, hemicellulose, lignin, protein and oil. Energy Convers Manag 2020;216:112777. https://doi.org/10.1016/j.enconman.2020.112777.

[36] Mariuzza D, Lin J-C, Volpe M, Fiori L, Ceylan S, Goldfarb JL. Impact of Co-Hydrothermal carbonization of animal and agricultural waste on hydrochars' soil amendment and solid fuel properties. Biomass and Bioenergy 2022;157:106329. https://doi.org/10.1016/j.biombioe.2021.106329.

[37] Wilcox RR. Introduction to robust estimation and hypothesis testing. Academic press; 2011.

[38] Vyazovkin S, Chrissafis K, Di Lorenzo ML, Koga N, Pijolat M, Roduit B, et al. ICTAC Kinetics Committee recommendations for collecting experimental thermal analysis data for kinetic computations. Thermochim Acta 2014;590:1–23. https://doi.org/10.1016/j.tca.2014.05.036.